RSC Advances

ROYAL SOCIETY OF CHEMISTRY

www.rsc.org/advances

Table of Contents

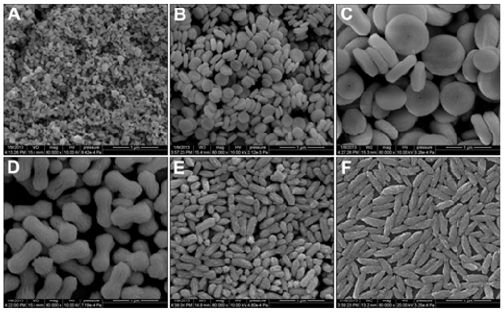

Diverse LnF_3–Ag hybrid architectures as substrates exhibit superior SERS performance and excellent detection sensibility for analytes.

Generalized Green Synthesis of Diverse LnF_3–Ag Hybird Architectures and Their Shape-dependent SERS Performances

Maofeng Zhang[a,b], Aiwu Zhao[a,b]*, Da Li[a], Henghui Sun[a], Dapeng Wang[a], Hongyan Guo[a], Qian Gao[a], Zibao Gan[a], Wenyu Tao[a]

a. Institute of Intelligent Machines, Chinese Academy of Sciences, Hefei, 230031, P. R. China
b. State Key Laboratory of Transducer Technology, Chinese Academy of Sciences, Hefei, 230031, P. R. China
** Corresponding author: E-mail: awzhao@iim.ac.cn*

Abstract

This paper reports the generalized green synthesis of a series of LnF_3–Ag (Ln = Nd, Sm, Eu, Tb) hybrid architectures with tunable shape, surface feature, and composition. These intriguing hybird structures are formed through the uniform magnetron sputtering of silver (Ag) nanoparticles on LnF_3 micro-supporters. The LnF_3–Ag surfaces are corrugated with high-density and numerous Ag nanogaps (which can serve as Raman active ‘hot spots’, to amplify the Raman signal), providing the sound reliability and reproducibility of Raman detection. We find that the special spindle structure of TbF_3–Ag particles display the highest Raman enhancement efficiency compared to disk-, pancake-, peanut-, and rice-like structures. These experimental observations are in good agreement with the theoretical calculation by using the three-dimensional finite difference time domain (3D-FDTD) method. It is found that the produced LnF_3–Ag composites are robust and efficient SERS substrate for high sensitivity detection of molecular adsorbates. Raman results show that the limit of detection (LOD) for crystal violet (CV), p-aminothiophenol (PATP) and Rhodamine 6G (R6G) of the optimized TbF_3–Ag spindles substrate are as low as 10^{-11} M, 10^{-10} M and 10^{-14} M, respectively, which meets the requirements for ultratrace detection of analytes. In addition, the LnF_3–Ag substrates are stable and can be produced with high reproducibility, which shows great potential applications for universal SERS substrates in practical SERS detections.

Keywords: Ag, rare-earth, Fluoride, Synthesis, Surface-enhanced Raman scattering (SERS) spectroscopy

1. Introduction

Surface-enhanced Raman scattering (SERS) spectroscopy have given birth to a powerful and versatile novel analytical tool due to its high sensitivity, specificity, and fingerprint effect in the detection of analysts,[1-4] thus has tremendous potential for chemical and biomolecular sensing and identification.[5,6] SERS can offer an enormous enhancement (10^{13}-10^{14} orders) over traditional Raman signal intensity, which enables this technique for trace or even single molecule level detection of proteins,[7] anthrax,[8] DNA,[9] explosives,[10] and environmental contaminants.[11] It is widely accepted that two mechanisms are responsible for such an enormous Raman enhancement: the electromagnetic (EM) mechanism and the chemical mechanism.[12-14] The EM mechanism, which is caused by the strong surface plasmon resonance (SPR) in rough metal surfaces excited by the incident light contributes the majority to the SERS enhancement. Since the SPR are extremely size- and shape-sensitive, the particles with the shape's characteristics of high local curvature, presence of sharp points, protrusions, and large aspect ratio are very interesting for SERS applications. Thus, the particles like disks, cubes, rods, prisms, stars, and flowers which can effectively amplify the electric field have attracted great interests.[15-20] Recently, special attention has been paid to rice-shaped metallic nanomaterials.[21-23] The excitation of the longitudinal nanorice plasmon gives rise to enormous local field enhancements exploitable for SERS. However, the key to perform these SERS applications is the fabrication of SERS active substrates with large SERS enhancement, high sensitivity, fine uniformity, good reproducibility, and biocompatibility.

Driven by the potential applications, tremendous efforts have been devoted to developing new techniques that can be used to synthesize SERS-active substrates.[24-26] Many researches have been focused on optimizing the host materials, and significant signal improvements have been reported via different approaches. For example, electron beam lithography [27] and nanosphere lithography [28] is developed to generate well-controlled SERS substrates with high SERS enhancement factors. But the cost of the required instrumentation hinders their wider application. Silver or gold has been deposited on different nanoporous templates such as TiO_2 [29] and Al_2O_3 [30] with notable SERS effects being obtained. However, fabrication of these substrates requires a relatively complicated process. And the seed growth and coating methods were employed to immobilize Au or Ag nanoparticles onto diverse supports to obtain the desired SERS substrates. While the synthesis process may introduce organics, surfactants or biomolecules, which may bring extra interferential bands in the SERS measurements, especially if the target analytes have a similar Raman spectral response to the agents. Despite the significant progresses, it seems that a facile, green, and cost-effective fabrication of SERS-active substrates with large-area surface morphology uniformity, stability, high enhancement factor and good reproducibility, still remains challenging. Recently, physical sputtering was exploited as a simple, straightforward, and inexpensive method for fabrication of Au or Ag nanostructures for high sensitivity SERS applications. For example, 3D hybrid silver nanocluster-decorated ZnO nanowire arrays were fabricated via depositing Ag nanoclusters onto ZnO nanowire arrays by using a gas-aggregation-type nanocluster beam source;[31] and the fabrication of arrays of vertically aligned cone-shaped ZnO nanorods decorated with Ag NPs as a highly sensitive and uniform 3D SERS substrate via ion-sputtering.[32] Very recently, a simple Ar^+-ion sputtering route has been developed to fabricate silver nanoneedles arrays on silicon substrates for SERS-active substrates to detect trace-level illicitly sold narcotics.[33] However, it is still necessary to explore other materials as templates to directly synthesize Au or Ag decorated hybrid structures.

Interestingly, rare-earth fluorides (with high chemical stability, high biocompatibility and low toxicity) emitters decorated by rough noble metal have been widely investigated for surface-enhanced fluorescence and used in bioassay systems.[34-36] For example, $NaYF_4$:Yb/Tm nanoparticles were surface-decorated with 1–2 nm Au seeds, increasing the emission intensity by 2.5 times;[37] and $NaYF_4$:Yb/Er nanocrystals assembled with gold nanospheres achieved a plasmon-enhanced upconversion enhancement factor of 3.8.[38] More recently, a maximum upconversion luminescence enhancement of 14.4-fold was observed in the $NaYF_4$:Yb,Er@SiO_2@Ag core–shell nanocomposites.[39] By contrast, further growth and coalescence of these Au or Ag islands led to the formation of an Au or Ag shell, which can greatly suppress the emission, possibly due to the strong scattering of excitation irradiation. These findings open a new pathway to rationally modulate the emission and quenching, and can open up new opportunities for energy harvesting and conversion. Inspired by this thought, using LnF_3 particles as the energy donor and gold or silver nanoparticles as the energy acceptor, to synthesize LnF_3–Ag hybrid structures as SERS-active substrates is very likely a feasible and alternative strategy. However, there is few report on the SERS performances and applications of rare-earth fluorides decorated by noble metals up to now. In this paper, we report a far simple and high efficient route based on magnetron sputtering technique to fabricate SERS-active substrates consisting of LnF_3–Ag composites and with an ideal reproducible surface morphology where strong SERS signals can be generated. Six types of fluoride particles, NdF_3 disk, SmF_3 disk, EuF_3 pancake, TbF_3 peanut, TbF_3 rice, and TbF_3 spindle are firstly fabricated by a simple sonochemical method. Then, the particles are transferred onto the silicon wafer to form a monolayer and are used as the initial templates to allow sputtering Ag NPs. These types of LnF_3–Ag composites are expected to generate different localized surface plasmon resonances (LSPRs). The LSPR-induced electromagnetic field enhancements in the six types of LnF_3–Ag composites will result in different enhancements of the Raman signal. Hence the SERS enhancement abilities and the electromagnetic field distribution are investigated with experiments combined with three-dimensional finite difference time domain (FDTD) simulation in order to screen for which one has the strongest SERS enhancement. It is found that the TbF_3–Ag spindles show the highest enhancement efficiency and high SERS sensitivity to rhodamine 6G (R6G), crystal violet (CV) and p-aminothiophenol

(PATP). And an extremely low concentration of 10^{-14} M for R6G and 10^{-11} M for CV can be detected. It is noted that the obtained LnF_3–Ag composites are stable and can be large-scale produced with high repeatability and good uniformity at a minimal cost. Moreover, the formed silicon wafer SERS substrates can be cut into pieces to directly detect diverse target analytes, which shows great potential for the rapid ultratrace detection of analytes.

2. Experimental Section

2.1. Sample Preparation

Materials. Rare-earth chloride hydrated ($LnCl_3$ $6H_2O$, Ln=Nd, Sm, Eu, Tb), Sodium tetrafluoroborate ($NaBF_4$) and absolute ethanol were obtained from Shanghai Chemical Reagent Company (Shanghai, China). Crystal violet (CV), p-aminothiophenol (PATP) and Rhodamine 6G (R6G) were obtained from Sigma Company. The reagents were of analytical grade and used without further purification. Ultrapure water (>18.0MΩ cm) was purified using a millipore milli-q gradient system throughout the experiment.

Fabrication of diverse LnF_3 particles. The LnF_3 particles were synthesized by a sonochemical method under ambient conditions. In a typical procedure, 2 mmol of $LnCl_3$ $6H_2O$ was added to 30 mL of deionized water in a beaker, followed by mixing with 6 mmol of $NaBF_4$ aqueous solution. The mixture was sonicated under ultrasonic frequency of 28 kHz for 3 h. Ultrasonic irradiation was performed using an ultrasonic generator (KQ-100VDB, ultrasonic power of 100 W) with a stainless steel mesh screen. Different shapes of LnF_3 particles were obtained by changing ultrasonic frequency, time, or reagents. For example, NdF_3 disk, SmF_3 disk, EuF_3 pancake and TbF_3 peanut were synthesized under the same ultrasonic frequency of 28 kHz at ambient temperature for 3 h. TbF_3 rices were prepared at an ultrasonic frequency of 100 kHz while keeping other conditions constant. TbF_3 spindles were prepared by substituting the same amount of $NaBF_4$ for NH_4F under ultrasonic frequency of 28 kHz for 3 h. The products were carefully collected and washed with distilled water and absolute ethanol several times to remove impurities. Finally, the products were redispersed in 1 mL ethanol for further use.

Synthesis procedures for the LnF_3–Ag composites. LnF_3–Ag composites with different thickness were prepared in a magnetron sputtering system (PECVD-400). A single target of Ag (99.99%) was sputtered in high purity Ar gas. Silicon wafer was used as substrates, and they were surface functionalized prior to sputtering. Then, LnF_3 nanoparticles were ultrasonically dispersed in a ethanol solvent, and transfered onto silicon wafer (2 cm × 2 cm), yielding a self-assembled monolayer. After dried in the air, the silicon wafer was placed in the magnetron sputtering chamber (2 cm away from the Ag target) to allow sputtering small Ag nanoparticles. The sputtering system was evacuated to be a background pressure down to 1×10^{-5} Pa, and pure Ar gas (99.9995%) with required quantity was introduced through mass flow controllers to reach required sputtering pressure (0.5 Pa). The sputtering was operated at sputtering power of 50 W for different sputtering times. Last, the as-prepared samples were cut into pieces (2 mm × 2 mm) as SERS substrates. These SERS substrates were immersed in 0.2 mL of crystal violet (CV), p-aminothiophenol (PATP) and Rhodamine 6G (R6G) ethanol solutions of different concentrations for 12 h. The pieces were taken out, rinsed with ethanol and deionized water, and dried in air before the subsequent characterization.

2.2 Characterization

Field emission scanning electron microscope images were taken with a field emission scanning electron microscope (Quanta 200 FEG) operated at an accelerating voltage of 10.0 kV (ZYVEX, America). The Raman scattering spectra were conducted with a confocal microscopy DXR SmartRaman Spectrometer (Thermo Scientific) equipped with a CCD detector and a holographic notch filter. Radiation of 532 nm from an air-argon ion laser (Spectra-Physics model 163-C4260) was used for excitation. During SERS measurements, the laser light was vertically projected onto the samples with a resultant beam diameter of about 2 μm. And the SERS spectra were collected at 100 × objective. Ten spectra were acquired for each of the measurements, and the average one was selected for figure legends. The spectra in this paper were background subtracted.

3. Results and Discussion

3.1. The particle size and shape of the LnF_3 particles

Preparation of LnF_3–Ag composites involves two steps: Fabrication of LnF_3 particles and magnetron sputtering of Ag nanoparticles onto the LnF_3 particles. Fig. 1(A)-(D) show typical SEM images of the LnF_3 (Ln = Nd, Sm, Eu, Tb) particles synthesized under an ultrasonic frequency of 28 kHz at ambient temperature. They clearly reveal that a large quantity and good uniformity of LnF_3 particles with different shapes are achieved using this approach. Fig. 1A and B give the SEM images of small size of NdF_3 disks and large size of SmF_3 disks, respectively. The former has a mean diameter of ～90 nm and thickness of ～20 nm, and the later has an average diameter of ～330 nm and thickness of ～60 nm. Fig. 1C shows that large amount of pancake-like EuF_3 particles are produced. The as-prepared EuF_3 pancakes were rounded, consisting of a hollow core. The average overall dimension of these pancakes was ～680 nm and thickness of ～200 nm. Interestingly, TbF_3 peanuts with length of ～920 nm and maximal diameter of ～440 nm can be prepared at the same synthesis conditions (Fig. 1D). Moreover, TbF_3 rices and TbF_3 spindles can also be fabricated by simply modifying reaction conditions. Fig. 1E shows TbF_3 rices image prepared at an ultrasonic frequency of 100 kHz while keeping other conditions constant. It is observed that TbF_3 rices have a mean length of ～440 nm and maximal diameter of ～160 nm. And TbF_3 spindles with large aspect ratio (length of ～580 nm and diameter of ～140 nm) are prepared by substituting the same amount of $NaBF_4$ for NH_4F, as shown in Fig. 1F. It is noted that these uniform LnF_3 particles can be readily obtained in high amount through the present method. Besides, these LnF_3 particles are ultrasonically dispersed and transfered onto a silicon wafer to yield a self-assembled monolayer for the following magnetron sputtering of Ag nanoparticles, and further to form a large quantity of efficient SERS ‘hot spots’.

3.2. The formation process of the LnF_3–Ag composites

Magnetron sputtering of Ag nan was oparticles onto different sizes and shapes of LnF_3 particles carried out in a magnetron sputtering system. Fig. 2(A)-(F) gives SEM image of LnF_3–Ag composites obtained at the same sputtering power of 50 W and time of 130 s. It can be seen that a mass of Ag nanoparticles are assembled onto the surface of the LnF_3 particles to form a surface roughed silver shell, which achieves a more sensitive SERS substrate loaded with sufficient ‘hot spots’. To illustrate the morphology evolution process in the formation of the LnF_3–Ag composites, a series of detailed time-dependent experiments were carried out. Take TbF_3 peanut for example, the TbF_3–Ag composites were prepared at sputtering power of 50 W for different sputtering times from 10 to 160 s, as shown in Fig. S1. Within a short time of 10 s, sparsely silver nanoparticles size ranging from 6 to 30 nm were deposited on the surface of the TbF_3 peanuts. Increasing sputtering time to 40 s, a thin silver shell (thickness of about 8 nm) on the surface of TbF_3 peanuts particles were formed. As the sputtering time prolonging to 130 s, the silver shell thickness of the TbF_3 peanuts correspondingly increased to 28 nm. It was found that a longer sputtering time resulted in a thicker silver shell and a rougher TbF_3–Ag surface structure which might provide abundant efficient ‘hot spots’ to perform SERS detection and identification of analytes. However, further increase of the sputtering time over 160 s produced adhesive TbF_3 peanuts composites, and the the morphology of the original peanuts began to deform. It was observed that the optimised conditions for the construction of LnF_3–Ag composites were sputtering power of 50 W and time of 130 s.

3.3. SERS Performances of LnF_3–Ag composites

The performance of LnF_3–Ag composites as SERS-active substrates was initially investigated by using CV as target analyte. Fig.3 shows the SERS spectra of CV adsorbed on representative TbF_3–Ag peanut substrates obtained at different sputtering times. The same spectral pattern is observed in the SERS spectra of CV for concentration of 10^{-6} M. The bands at 915, 1170 and 1388 cm^{-1} are assigned to the ring skeletal vibrations, C–H in-plane bending vibrations and N-phenyl stretching of CV, respectively.[40] The bands at 1535, 1584 and 1617 cm^{-1} are attributed to ring C–C stretching.[41] It is observed that the SERS intensity increases with the increase of sputtering time and reaches a maximal value for 130 s, then decreases to some extent for 160 s. At the beginning of 10 s, only sparse silver nanoparticles were decorated onto the surface of TbF_3 peanuts which leads to the lowest SERS enhancement. As sputtering time prolongs, silver thickness and the number of silver nanoparticles increases which tends to form a large number of gaps or voids, providing more active sites where afford potential high density ‘hot spots’ to amplify the local electromagnetic fields as well as the Raman signal.[42] However, further increasing sputtering time, the newly formed gaps or voids were filled by silver nanoparticles which reduces the potential ‘hot spots’, thus lowers the SERS intensity. As expected, no intrinsic Raman signals and the fluorescence disturbance from the LnF_3 are observed in the experiments. This may be due to the following facts: (1) the strong SERS signal of CV effectively shields the intrinsic signals of LnF_3; (2) such a low excitation energy of 0.5 mW can effectively avoid auto-fluorescence from samples. (3) the formation of the silver shell greatly suppresses the fluorescence emission. These results indicate that LnF_3 as templates to prepare LnF_3–Ag composites with expected SERS properties have shown to be a feasible and alternative strategy.

Both computational and experimental studies have demonstrated that the shapes and sizes of metal nanostructures are the main factor in determining the LSPR, which facilitates their applications in ultrasensitive sensing and surface-enhanced Raman spectroscopy.[43-45] Herein, we employed the as-prepared NdF_3–Ag disks, SmF_3–Ag disks, EuF_3–Ag pancakes, TbF_3–Ag peanuts, TbF_3–Ag rices, and TbF_3–Ag spindles as SERS-active substrates to evaluate the shape and size effects on their SERS properties, using CV as the probe molecules. As shown in Fig. 4, it was found that the TbF_3–Ag rices and spindles showed stronger SERS signals as compared to the other shapes mainly due to the shaper corners and edges of these structures in comparison with the disks and pancakes. Recent studies had revealed that nanorices with sharper corners would give rise to enormous LSPR near their corners. Moreover, the TbF_3–Ag spindles with sharp tips exhibited superior SERS activity than the TbF_3–Ag rices. This is not difficult to understand by the lightning rod effect which causes the dipolar fields of the spindles to be concentrated near their tips.[46] For TbF_3–Ag peanuts, the SERS enhancement was still strong enough. Since nanoscale surface roughness also significantly increased local field enhancements on the surface of these hybird particles, which could achieve 10^6-10^7 SERS enhancements on individual particles. And the SmF_3–Ag pancakes with a cavity in the core gave stronger signals than that of NdF_3–Ag disks, possibly due to their better molecule capturing ability. For the same disk-shaped particles, the small sized NdF_3–Ag disks showed stronger Raman enhancement than large sized SmF_3–Ag disks due to their high specific surface area of small particle size, favoring the absorption of incident light and the capture of probe molecules. Overall, the TbF_3–Ag spindles showed the highest enhancement efficiency and the SmF_3–Ag disks showed the lowest enhancement efficiency.

To explain these experimental observations, the electric field enhancement of SERS-active LnF_3–Ag structures was estimated by using the three-dimensional finite-difference time-domain (3D-FDTD) method. Fig. 5 shows the electric field intensity distributions on excitation with a 532 nm wavelength of incident light, which corresponds to the wavelength of the experimental SERS measurements. In this calculation, the thickness of Ag film was assumed to be 28 nm and the incident light was linearly polarized. After the numerical calculations to the electric field intensity distributions of each shape with 3D-FDTD method,[47] the maximum electric field enhancement values of each shape were found to be 2.1 V/m, 1.2 V/m, 3.1 V/m, 4.6 V/m, 16.3 V/m, and 31.6 V/m, respectively. From the calculated results, the TbF_3–Ag spindles showed the highest calculated value of the maximum electric field intensity. For the TbF_3–Ag spindle-like structures (Fig. 2F), a highly enhanced electric field was localized at the two sharp tips of the spindle when the field was aligned with the longitudinal LSPR mode of the spindle, which may be due to the favorable orientation of the incident laser for the longitudinal LSPR mode and the strong longitudinal LSPR absorption. Furthermore, it should be noted that the maximum electric field intensity appeared around the sharp tip in the anisotropic structure, in agreement with previous reports showing that the electromagnetic field can be concentrated at the sharp tips of nanostructures.[48–50] The confined LSPR at these sharp tips generated 'hot spots' and resulted in the dominant contribution to the SERS intensity. Fig. 5A-F also present the different LnF_3-Ag size and shape's effects on the enhancement of the local electric field. The TbF_3–Ag rices exhibited lower maximum electric field intensity and the EuF_3–Ag pancakes showed the lowest maximum electric field intensity value. We find that these results are in good agreement with the experimental data.

3.4. LnF_3–Ag composites SERS substrate for high sensitive detection

In this study, the sensitive properties of the TbF_3–Ag spindles with maximum enhancement efficiency were selected as SERS substrates to detect several representative SERS-active analytes such as CV, PATP, and R6G to test its effect. Fig.6A demonstrates the results of SERS spectra with different concentrations on the substrate from 10^{-6} M to 10^{-11} M. The peaks at 915, 1170 1388 and 1617 cm^{-1} observed in our SERS spectrum can be attributed to CV. The spectral intensities and resolutions are decreased with diluting the concentrations of the target molecules. It is found that additional CV peaks still appeared at about 1170 and 1617 cm^{-1} at a low concentration of 10^{-11} M, which indicates that this SERS substrate is highly sensitive and promising for the detection of other target molecules. Hence, we examined the detection sensitivity of the as-obtained TbF_3–Ag spindles for the detection of PATP molecules. Fig. 6B shows the SERS spectra of PATP with different concentrations adsorbed on the TbF_3–Ag spindles substrate. The peaks at 1573, 1438, and 1390 cm^{-1} are attributed to PATP.[51,52] These results demonstrate that PATP can be well detected with TbF_3–Ag spindles SERS substrate in concentration ranges down to 10^{-10} M. Additionally, R6G was used to further demonstrate the detection sensitivity of the TbF_3–Ag spindles substrate. The SERS spectra of R6G with different concentrations adsorbed on the TbF_3–Ag spindles substrate are shown in Fig. 6C. The peaks from 580 to 1700 cm^{-1} are attributed to R6G signals; vibrations at 1182, 1309, 1362, 1507, and 1651 cm^{-1} are assigned to C–H in-plane bending, C–O–C stretching, and C–C stretching of the aromatic ring.[53] It is observed that TbF_3–Ag spindles substrate also exhibited high detection sensitivity for R6G and the LOD is decided to be 5×10^{-14} M. On this concentration level, single molecule detections by SERS can be achieved. These observations confirm that this kind of TbF_3–Ag spindles substrate can achieve the ultratrace detection of analytes.[54] Such a low LOD for R6G has previously been reported by us [55,56] and others. In the study of ultrasensitive trace detection by SERS, Ag colloids were used as active substrate to detect R6G and the practical LOD can reach to 3×10^{-14} M.[57] Moreover, silicon nanowires coated with Ag nanoparticles were also employed as SERS-active substrate, showing a large Raman scattering enhancement for rhodamine 6G (R6G) with a LOD of 10^{-14} M.[58]

In the study of signal enhancement of SERS and surface-enhanced resonance Raman scattering (SERRS) by the use of in situ synthesized silver colloid, in a lab-on-a-chip format, a LOD of ca. 5×10^{-14} M was observed for the model Raman active label (R6G).[59] R6G was found to give a strong surface enhanced Resonance Raman scattering (SERRS) signal, when excited at 532 nm. The difference in the LOD and the sensitivity can be explained by the fact that the R6G is giving a SERRS response, while that for CV and PATP is a SERS response. The important contribution of this work is to significantly reduce the practical LOD for target analytes adsorbed on the TbF_3–Ag spindles substrate. Therefore, the detection level of our product was suitable for ultratrace probing of other organic analytes.

While employing SERS technology to detect target molecules in the real use, the reproducibility and the stability of LnF_3–Ag SERS substrate must be validated. The SERS mapping is often used to estimate the reproducibility of SERS signals.[60] Fig. 6D shows a SERS spatial map composed of the intensity of the 1507 cm^{-1} band at the lowest concentration of R6G (5×10^{-14} M) adsorbed on the TbF_3–Ag spindles substrate. It can be seen that there is a homogeneous SERS response throughout the whole surface, with a scale of 40 μm. Except for some inevitable defect spots, most of them are between 1400 and 2000 counts with a relatively narrow distribution within 10 % deviation from the mean, which shows that our TbF_3–Ag spindles substrate is an excellent SERS substrate. Moreover, the corresponding spectra drawn from SERS map are shown in Fig. S2. Clear Raman peaks of R6G at 614, 1309, 1362, 1507, and 1651 cm^{-1} can be observed. The most obvious feature of these spectra is that the intensity of the peaks has some fluctuations. The interpretation of these fluctuations is that the number of detected R6G molecules is approaching the single molecule limit, and, therefore, a change by a single molecule either entering or leaving the scattering volume is a substantial fraction of the signal.[61] In addition to the strong SERS enhancement effect, the TbF_3–Ag spindles substrate are stable and can be produced with high reproducibility across the entire area, which shows great potential application for universal SERS substrates.

4. Conclusions

In summary, we have designed a generalized green route to the synthesis of LnF_3–Ag (Ln = Nd, Sm, Eu, Tb) hybrid architectures by sputtering Ag nanostructures on LnF_3 micro-supporters. The high-density and numerous Ag nanogaps can be formed at interparticle sites by controlling the magnetron sputtering parameters. The special spindle structure of TbF_3–Ag particles display the highest Raman enhancement efficiency compared to other structures, which is in good agreement with the theoretical calculation by using the 3D-FDTD method. It must be noted that the LnF_3–Ag composites are robust and can be used as efficient SERS substrate for high sensitivity detection of molecular adsorbates. The detection limits for CV, PATP and R6G of the optimized TbF_3–Ag spindles substrate are as low as 10^{-11} M, 10^{-10} M and 10^{-14} M, respectively, which meets the requirements for ultratrace detection of analytes. We believe that these TbF_3–Ag spindles could serve as ideal substrate for SERS applications and provide an excellent candidate for SERS analysis.

Acknowledgment. This work was supported by the National Natural Science Foundation of China (No. 61378038), the National Natural Science Foundation of China (No. 61205150), the National Basic Research Program of China (2011CB302103), and the State Key Laboratories of Transducer Technology for financial support.

Notes and references

1 S. Lal, N. K. Grady, J. Kundu, C. S. Levin, J. B. Lassiter and N. J. Halas, *Chem. Soc. Rev.*, 2008, **37**, 898–911.

2 S. Y. Lee, L. Hung, G. S. Lang, J. E. Cornett, I. D. Mayergoyz and O. Rabin, *ACS Nano*, 2010, **4**, 5763–5772.

3 X. H. Xia, J. Zeng, B. McDearmon, Y. Q. Zheng, Q. G. Li and Y. N. Xia, *Angew. Chem., Int. Ed.*, 2011, **50**, 12542–12546.

4 L. Su, W. Z. Jia, D. P. Manuzzi, L. C. Zhang, X. P. Li, Z. Y. Gu and Y. Lei, *RSC Adv.*, 2012, **2**, 1439–1443.

5 J. F. Li, Y. F. Huang, Y. Ding, Z. L. Yang, S.B. Li, X. S. Zhou, F. R. Fan, W. Z, Z.Y. Zhou, D.Y. Wu, B. Ren, Z. L. Wang and Z. Q.Tian, *Nature*, 2010, **464**, 392–395.

6 Y. Yang, Z.Y. Li, K. Yamaguchi, M. Tanemura, Z. R. Huang, D. L. Jiang,Y. H. Chen, F. Zhou and M. Nogami, *Nanoscale*, 2012, **4**, 2663–2669.

7 X. M. Kong, Q. Yu, X. F. Zhang, X. Z.Du, H. Gong ang H. Jiang, *J. Mater. Chem.*, 2012, **22**, 7767–7774.

8 K. Ryu, A. J. Haes, H. Y. Park, S. Nah, J. Kim, H. Chung, M. Y. Yoon and S. H. Han, *J. Raman Spectrosc*., 2010, **41**, 121–124.

9 M. Li, S. K. Cushing, H. Y. Liang, S. Suri, D. L. Ma and N. Q. Wu, *Anal. Chem.*, 2013, **85**, 2072–2078.

10 A. Chou, E. Jaatinen, R. Buividas, G. Seniutinas, S. Juodkazis, E. L. Izake and P. M. Fredericks, *Nanoscale*, 2012, **4**, 7419–7424

11 Y. Zhou, J. Chen, L. Zhang and L. B. Yang, *Eur. J. Inorg. Chem.*, 2012, 3176–3182.

12 M. Moskovits, *Rev. Mod. Phys*., 1985, **57**, 783–826.

13 A. Campion and P. Kambhampati, *Chem. Soc. Rev.*, 1998, **27**, 241–250.

14 X. T. Wang, W. S. Shi, G. W. She and L. X. Mu, *J. Am. Chem. Soc.*, 2011,**133**, 16158–16523.

15 C. Liusman, H. Li, G. Lu, J. Wu, F. Boey, S. Z. Li and H. Zhang, *J. Phys. Chem. C*, 2012, **116 (18)**, 10390–10395.

16 M. Rycenga, M. R. Langille, M. L. Personick, T. Ozel and C. A. Mirkin, *Nano Lett.*, 2012, **12 (12)**, 6218–6222.

17 Z. L. Huang, G. W. Meng, Q. Huang, B. Chen, C. H. Zhu and Z. Zhang, *J. Raman Spectrosc.*, 2013, **44**, 240–246.

18 N. Cathcart and V. Kitaev, *Nanoscale*, 2012, **4**, 6981–6989.

19 L. Vigderman and E. R. Zubarev, *Langmuir*, 2012, **28 (24)**, 9034–9040.

20 Q. Li, Y. Y. Jiang, R. C. Han, X. L. Zhong, S. Y. Liu, Z. Y. Li, Y. L. Sha and D. S. Xu, *Small*, 2013, **9**, 927–932.

21 B. J. Wiley, Y. Chen, J. M. Mclellan, Y. Xiong, Z. Y. Li, D. Ginger and Y. N. Xia, *Nano Lett.*, 2007, **7**, 1032–1036.

22 H. Wei, A. Reyes-Coronado, P. Nordlander, J. Aizpurua and H. X. Xu, *ACS Nano*, 2010, **4**, 2649–2654.

23 L. Chen, H. K. Seo, Z. Mao, Y. M. Jung and B. Zhao, *Anal. Methods*, 2011, **3**, 1622–1627.

24 J. B. Song, J. J. Zhou and H. W. Duan, *J. Am. Chem. Soc.*, 2012, **134**, 13458−13469.

25 X. L. Liu, J. Zhou, Z. X. Xue, J. Gao, J. X. Meng, S. T. Wang and L. Jiang, *Adv. Mater.*, 2012, **24**, 3401–3405.

26 H. Y. Wu, C. J. Choi and B. T. Cunningham, *Small*, 2012, **8**, 2878–2885.

27 W. S. Yue, Z. H. Wang, Y. Yang, L. Q. Chen, A. Syed, K. C. Wong and X. B. Wang, *J. Micromech. Microeng.*, 2012, **22**, 125007–125016.

28 J. Aizpurua, P. Hanarp, D. S. Sutherland, M. Käll, G. W. Bryant and F. J. García de Abajo, Phys. Rev. Lett., 2003, **90(5)**, 057401–057403.

29 M. Pisareka, A. Roguskaa, A. Kudelskic, M. Andrzejczukb, M. J. Czachor and K. J. Kurzydłowski, *Mater. Chem. Phys.*, 2013, **139**, 55–65.

30 B. Mondal and S.K. Saha, *Chem. Phys. Lett.*, 2010, **497**, 89–93.

31 S. Deng, H. M. Fan, X. Zhang, K. P. Loh, C. L. Cheng, C. H. Sow and Y. L. Foo, *Nanotechnology*, 2009, **20**, 175705–175710.

32 H. B. Tang, G. W. Meng, Q. Huang, Z. Zhang, Z. L. Huang and C. H. Zhu, *Adv. Funct. Mater.*, 2012, **22**, 218–224.

33 Y. Yang, Z. Y Li, K. Yamaguchi, M. Tanemura, Z. R. Huang, D. L. Jiang, Y. H. Chen, F. Zhou, M. Nogami, Y. Yang, *Nanoscale*, 2012,**4**, 2663–2669.

34 C. D. Geddes and J. R. Lakowicz, *J. Fluoresc.*, 2002, **12**, 121–129.

35 K. A. Willets and R. P. Van Duyne, *Annu. Rev. Phys. Chem.*, 2007, **58**, 267–297.

36 W. Feng, L. D. Sun and C. H. Yan, *Chem. Commun.*, 2009, 4393–4395.

37 H. Zhang, Y. J. Li, I. A. Ivanov, Y. Q. Qu, Y. Huang and X. F. Duan, *Angew. Chem., Int. Ed.*, 2010, **49**, 2865–2868.

38 S. Schietinger, T. Aichele, H. Q. Wang, T. Nann and O. Benson, *Nano Lett.*, 2010, **10**, 134–138.

39 P. Y. Yuan, Y. H. Lee, M. K. Gnanasammandhan, Z. P. Guan, Y. Zhang and Qing-Hua Xu, *Nanoscale*, 2012, **4**, 5132–5137.

40 D. H. Zhang, X. H. Liu and X. Wang, *J. Mol. Struct.*, 2011, **985**, 82–85.

41 R. Sanci and M. Volkan, *Sensor. Actuat. B-Chem.*, 2009, **139**, 150–155.

42 J. Rodríguez-Fernández, A. M. Funston, J. Pérez-Juste, R. A. Álvarez-Puebla, L. M. Liz-Marzán and P. Mulvaney, *Phys. Chem. Chem. Phys.*, 2009, **11**, 5909–5914.

43 K. L. Kelly, E. Coronado, L. L. Zhao, G. C. Schatz, *J. Phys. Chem. B* 2003, **107**, 668–677.

44 E. Hutter, J. H. Fendler, *Adv. Mater.* 2004, **16**, 1685–1706.

45 K. L. Shuford, J. Lee, T. W. Odom, G. C. Schatz, *J. Phys. Chem. C* 2008, **112**, 6662–6666.

46 P. F. Liao and A. Wokaun, *J. Chem. Phys.*, 1982, **76**, 751–752.

47 K. Kunz and R. Luebbers, The Finite Difference Time Domain Method for Electromagnetics, CRC press, New York, 1993.

48 J. Henzie, J. E. Barton, C. L. Stender and T. W. Odom, *Acc. Chem. Res.*, 2006, **39**, 249–57.

49 C. G. Khoury and T. Vo-Dinh, *J. Phys. Chem. C* 2008, **112**, 18849–59.

50 S. K. Dondapati, T. K. Sau, C. Hrelescu, T. A. Klar, F. D. Stefani and J. Feldmann, *ACS Nano*, 2010, **4**, 6318–22.

51 K. Kim, H. B. Lee, J. K. Yoon, D. H. Shin and K. S. Shin, *J. Phys. Chem. C*, 2010, **114**, 13589–13595.

52 H. L. Liu, L. B. Yang, H. W. Ma, Z. M. Qi and J. H. Liu, *Chem. Comm.*, 2011, **47**, 9360–9362.

53 L. L. Sun, Y. H. Song, L. Wang, C. L. Guo, Y. J. Sun, Z. L. Liu and Z. Li, *J. Phys. Chem. C*, 2008, **112**, 1415–1422.

54 L. H. Qian, X. Q. Yan, T. Fujita, A. Inoue and M. W. Chen, *Appl. Phys. Lett.*, 2007, **90**, 153120–153122.

55 M. F. Zhang, A. W. Zhao, H. Y. Guo, D. P. Wang, Z. B. Gan, H. H. Sun, D. Li and M. Li, *CrystEngComm*, 2011, **13**, 5709–5717.

56 Z. B. Gan, A. W. Zhao, M. F. Zhang, D. P. Wang, H. Y. Guo, W. Y. Tao, Q. Gao, R. R. Mao and E. H. Liu, *J. Nanopart. Res.*,

2013, **15**,1954–1966.

57 P. Etchegoin, R. C. Maher, L. F. Cohen, H. Hartigan, R. J. C. Brown, M. J. T. Milton and J. C. Gallop, *Chem. Phys. Lett.*, 2003, **375**, 84–90.

58 E. Galopin, J. Barbillat, Y. Coffinier, S. Szunerits, G. Patriarche and Rabah Boukherroub, *ACS Appl. Mater. Inter.*, 2009, **1**, 1396–1403.

59 R. Wilson, S. A. Bowden, J. Parnell and J. M. Cooper, *Anal. Chem.*, 2010, **82**, 2119–2123.

60 C. Farcau and S. Astilean, *J. Phys. Chem. C*, 2010, **114**, 11717–11722.

61 K. Kneipp, Y. Wang, H. Kneipp, L. T. Perelman, I. Itzkan, R. R. Dasari, M. S. Feld, *Phys.Rev. Lett.*, 1997, **78**, 1667–1670.

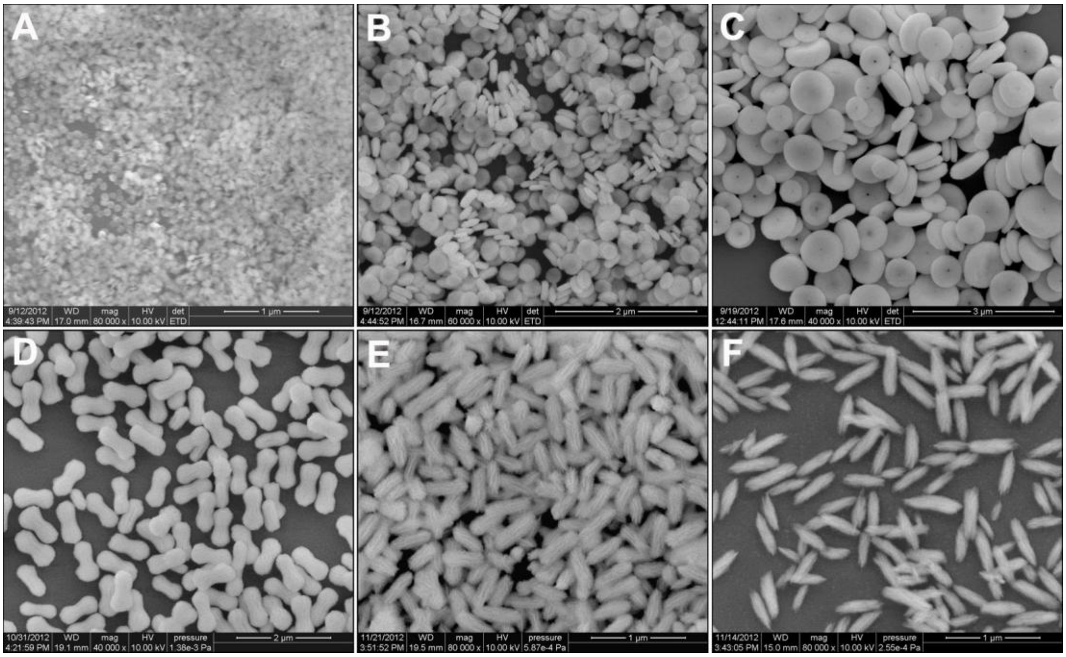

Fig.1 SEM images of (A) NdF_3 disk, (B) SmF_3 disk, (C) EuF_3 pancake, (D) TbF_3 peanut, (E) TbF_3 rice, and (F) TbF_3 spindle.

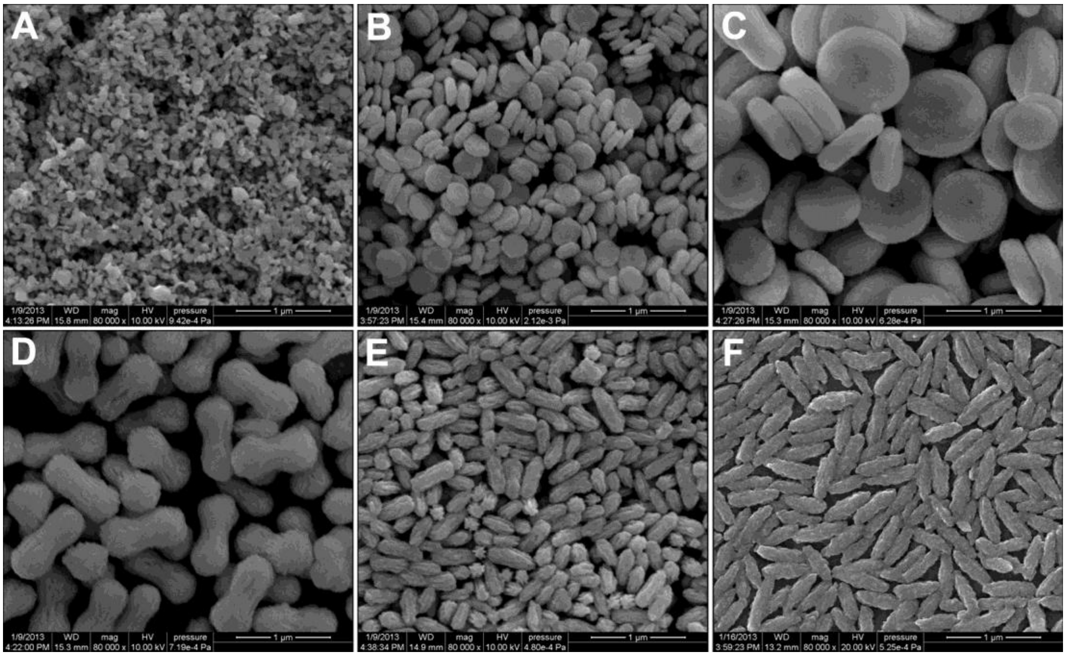

Fig.2 SEM images of (A) NdF_3–Ag disk, (B) SmF_3–Ag disk, (C) EuF_3–Ag pancake, (D) TbF_3–Ag peanut, (E) TbF_3–Ag rice, and (F) TbF_3–Ag spindle prepared at sputtering power of 50 W for 130 s.

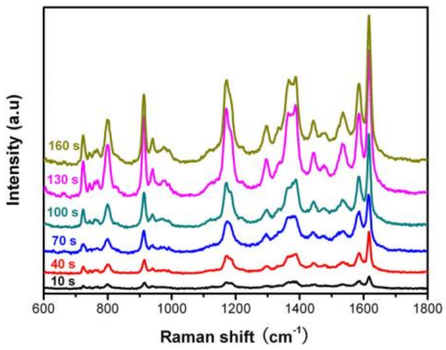

Fig. 3 SERS spectra of CV (10^{-6} M) adsorbed on TbF$_3$–Ag peanut substrates prepared at varied sputtering times. The excitation power was 0.5 mW and the integration time was 1 s.

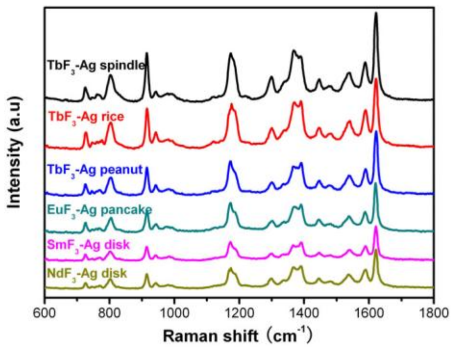

Fig. 4 SERS spectra of CV (10^{-6} M) adsorbed on different LnF$_3$–Ag composites substrates. All the LnF$_3$–Ag composites were prepared at the same sputtering power of 50 W for 130 s. The excitation power was 1 mW and the integration time was 5 s.

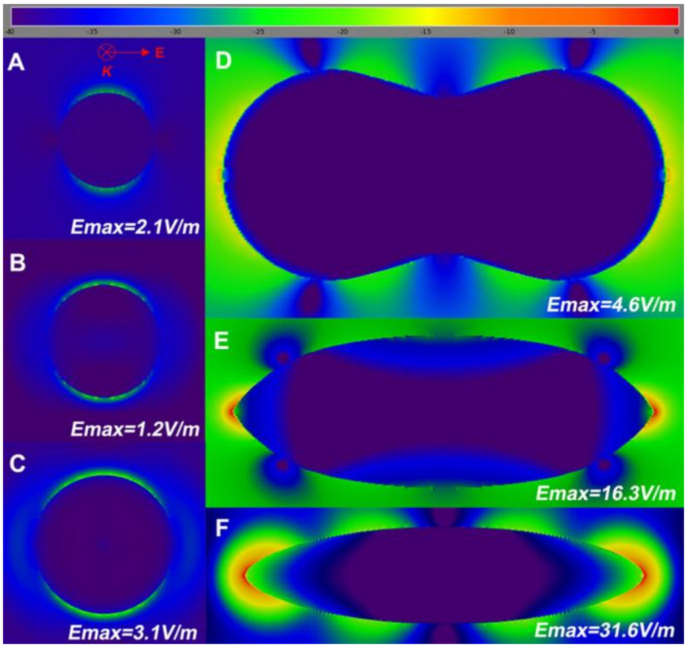

Fig. 5 Calculated electric field intensity distributions excited by an incident light with linearly polarized plane wave (λ = 532 nm) with different morphologies of NdF_3–Ag disks (A), SmF_3–Ag disks (B), EuF_3–Ag pancakes (C), TbF_3–Ag peanuts (D), TbF_3–Ag rices (E), and TbF_3–Ag spindles (F), respectively.

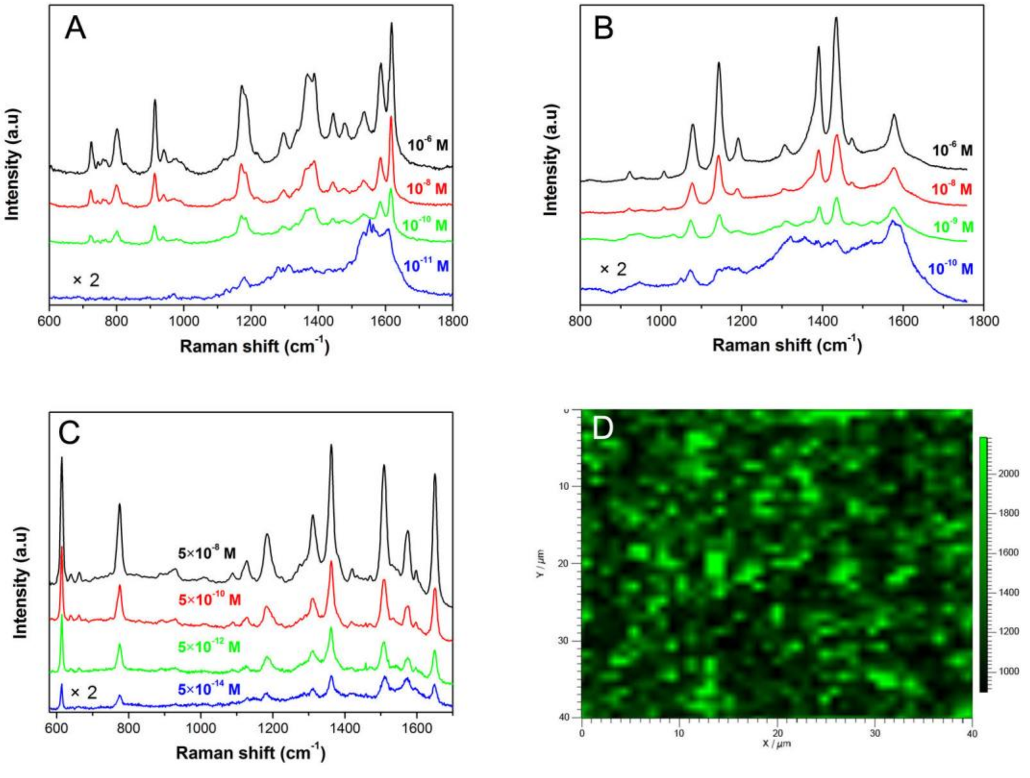

Fig. 6 SERS spectra obtained from different concentrations of CV (A), PATP (B), and R6G (C) adsorbed on TbF_3–Ag spindles substrates; (D) SERS map (40 μm × 40 μm) of the 1507 cm^{-1} band of R6G observed from TbF_3–Ag spindles substrate.